IEEE Access
Multidisciplinary | Rapid Review | Open Access Journal

Received May 28, 2021, accepted June 25, 2021, date of publication June 30, 2021, date of current version July 13, 2021.

Digital Object Identifier 10.1109/ACCESS.2021.3093530

A Short and Light, Sparse Dipolar Halbach Magnet for MRI

AARON R. PURCHASE[1], LOGI VIDARSSON[2], KEITH WACHOWICZ[1], PIOTR LISZKOWSKI[3,4], HONGWEI SUN[1], GORDON E. SARTY[5], JONATHAN C. SHARP[1], AND BOGUSLAW TOMANEK[1,6]

[1]Division of Medical Physics, Department of Oncology, University of Alberta, Edmonton, AB T6G 1Z2, Canada
[2]LT Imaging, Toronto, ON M4J 3B3, Canada
[3]Faculty of Physics and Applied Computer Science, AGH University of Science and Technology, 30-059 Kraków, Poland
[4]MRI-Tech Sp. z o.o., 30-209 Kraków, Poland
[5]Division of Biomedical Engineering, University of Saskatchewan, Saskatoon, SK S7N 5A2, Canada
[6]Institute of Nuclear Physics, Polish Academy of Sciences, 31-342 Kraków, Poland

Corresponding author: Boguslaw Tomanek (tomanek@ualberta.ca)

This work was supported in part by the Natural Sciences and Engineering Research Council of Canada (NSERC) Discovery under Grant RGPIN-2020-04414.

ABSTRACT Recently designed dipolar Halbach magnets used in portable MRI systems are much lighter and more compact than standard permanent or superconductive magnets. However, improved designs and manufacturing techniques aiming at lower weight and smaller external size are an area of continual interest especially for application to space flight. Most Halbach magnet design techniques aim to optimize homogeneity suitable for MRI over a diameter-spherical volume (DSV) that requires the aspect ratio (length/inner diameter) to be larger than 1.5:1. Furthermore, current magnet construction techniques often use low-coercivity magnetic pieces and imperfect formers that produce a mismatch in the intended designs. As a result, Halbach magnets require complex shimming methods to improve the magnetic field homogeneity, causing further size and weight increase. Here, we propose to reduce the weight and the aspect ratio of the Halbach magnet by optimizing homogeneity over a cylindrical region of interest (ROI) rather than a DSV, applying a genetic algorithm, high-coercivity ferromagnets (N40UH) and a robust construction technique. The assembled 67 mT magnet, with aspect ratio $\sim$ 1:1, produces almost identical homogeneity (11152 ppm) as simulations (11451 ppm) within a 12.7 cm diameter, 1 cm long cylinder ROI. The magnet structure was 3D printed ring-by-ring and assembled coaxially. The magnet can be disassembled for transportation.

INDEX TERMS MRI, magnets, magnetic field homogeneity, permanent magnet array.

I. INTRODUCTION

Magnetic resonance imaging (MRI) provides the highest soft-tissue contrast images for an extensive range of diseases such as cancer, osteoporosis, or neuro-disorders compared to other diagnostic imaging modalities. Unfortunately, MRI remains a generally inaccessible medical technology worldwide due to many factors such as extensive costs of purchase and maintenance, complexity, weight, size, geographical access limitations and a large physical space requirement [1]–[4]. Magnets and gradient subsystems are significant contributors to MRI inaccessibility due to their weight, size and price [4], [5]. These factors also prevent MRI from being used in space for the study of the effect of space travel on the human body.

MRI system costs, weight and size are primarily associated with the magnet [4], [5]. Common clinical superconductive magnets (>1.0 T) weigh 3-6 tons, have larger than 2 m outer diameter and are 2 m or more long [5], [6]. Standard permanent magnets ($\sim$0.2 T) such as the 4-post or C-shape provide open access for patients but are also heavy ($\sim$10 tons) [5], [7]. Regardless of the design, the magnet must also maintain very high magnetic field homogeneity ($\sim$10 ppm peak-to-peak) over a large diameter-spherical-volume (DSV) ($\sim$50 cm) [5], [6]. Unlike superconducting and bi-planar permanent magnets, Halbach magnets are lightweight (yoke-less), have a low footprint, and are a low-cost alternative to standard MRI magnets [6], [8]. Yet, so far,

The associate editor coordinating the review of this manuscript and approving it for publication was Jinhua Sheng.

their MRI applications are limited due to large magnetic field inhomogeneities [9]–[12]. Analytical solutions of the magnetic field equations showed that a 4:1 aspect ratio (length to inner diameter) provides a reasonable homogeneity (∼1000 ppm before shimming) for MRI but such a long magnet is heavy and claustrophobic, hence its limited clinical applications [13]. A shorter magnet (aspect ratio ∼2:1) generates an inhomogeneity of ∼10,000 ppm requiring complex design approaches and sophisticated shimming techniques [9], [10], [13], [14]. In Halbach magnets with aspect ratio <1.5:1, the produced inhomogeneity becomes too large (>100,000 ppm) for imaging [13], [15]. Additionally, more than 20 magnetized blocks around the cylinder must be used to rectify the impact of the segmented magnetization on homogeneity [12], [13]. Several research groups have proposed new approaches to improve the homogeneity of a short and segmented Halbach magnet, by optimizing block size and shape [16]–[18], diameters of rings [9], [10], elliptical arrangement of blocks [19], spacing between rings [20], magnetization directions of blocks [19], [21], or material remanence and coercivity [22]–[25]. Analytical approaches and finite element simulations have not considered variations in magnetic properties of the blocks (magnetization strength and direction), their sizes and inaccuracies in positions of the blocks in the magnet housing or instability of the field due to temperature fluctuations [9]–[11], [22]–[24]. As a result, constructed magnets have even higher inhomogeneity than expected from design simulations.

So far, homogeneity of superconducting and bi-planar permanent MRI magnets have been optimized within a DSV [6]. This allows MRI over a large region of interest (ROI) using gradients of the magnetic field with selective radiofrequency (RF) pulses [26], [27]. Unfortunately, optimization of homogeneity over the spherical volume when used in the design of portable Halbach magnets prevents the construction of magnets with low aspect ratio (<1.5:1) suitable for MRI. To deal with the inhomogeneities, RF pulses with a specific bandwidth (BW) can be applied allowing excitation of the region with inhomogeneities corresponding to the BW. For example, Perlo *et al.* (2004) achieved a set of 1 mm thick 2D MR images using a highly-inhomogeneous single-sided permanent magnet by exploiting the magnet's sensitive volumes [28]. We therefore expect a cylindrical ROI can be considered for imaging rather than the entire DSV. The thin cylindrical region would define a single selected natural slice [29] for a two-dimensional Transmit Array Spatial Encoding (TRASE) imaging scheme [30], [31].

Recent advancements in low field (LF) MRI hardware and imaging techniques, providing good soft tissue contrast but with low signal-to-noise (SNR), proves that further reduction of associated costs, weight, size and complexity of the MRI system is indeed possible [9], [10], [22]–[24]. For example, O'Reilly *et al.* (2021) constructed a portable (∼105 kg), low-field (∼50 mT) MRI system based on a new Halbach magnet optimization technique as well as hardware and software improvements intended for imaging of hydrocephalus in children with a material price below $20k [9], [10]. The group used finite element simulation and a genetic algorithm (GA) to optimize diameters of 23 rings in a sparse Halbach array for maximum field homogeneity (400 ppm) over a 20 cm DSV [9], [10]. However, after construction, due to the warping of water-cut Plexiglas formers, the measured field homogeneity was only 13,000 ppm within the DSV [9]. A shimming system requiring a large number of small permanent magnets was used to improve the B_0 homogeneity resulting in ∼2500 ppm over the DSV [9], [10]. 3D MR images of the knee and brain were obtained at 2 mm isotropic resolution in less than 12 minutes using this system [10]. Furthermore, Cooley *et al.* (2018) constructed a portable, low-field (∼80 mT) adult brain MRI scanner based on the novel rotational spatial encoding method (rSEM) [22], [23]. The group used the frequency swept 3D rapid acquisition and relaxation enhancement (RARE) pulse sequence with the inhomogeneous B_0 field to avoid a conventional MRI readout gradient and associated hardware [24]. The magnetic field was optimized to a 20 cm DSV, resulting in a magnet weight of 122 kg, 52 cm outer diameter, 35 cm inner diameter and 40 cm long [24]. The group reported variations in NdFeB size, magnetic properties and former imperfections, causing differences between the constructed and simulated Halbach magnet field over the DSV [22]–[24]. Regardless of non-linearity in the built-in B_0 gradient field, 3D MR in-vivo images of an adult brain were obtained in 16 minutes [12].

Both above-mentioned portable MRI systems show significant advancements in MR image quality in compact LF MRI systems, such as substantial reduction of field distortions through model-based reconstruction rather than conventional Fourier-based techniques [24], [32]. Unlike these methods, the recently introduced encoding method called TRASE uses the phase gradients of the RF field to spatial encode signal rather than applying a switching B_0 gradient or a built-in rotational spatial encoding field [30], [31]. Therefore, TRASE removes the need for the entire B_0 gradient system and, additionally, relaxes the main magnet homogeneity requirement, potentially increasing the compact and portable nature of current low-cost LF MRI systems. Recent developments of TRASE hardware enabled sub-millimeter 1D resolution (0.33 mm/pixel) in ∼8.5 minutes using a conventional 0.2 T bi-planar permanent magnet with a twisted-solenoid RF coil set [33], [34], a custom-made multi-channel RF amplifier [35], improved image reconstruction techniques [36]–[38] and a custom MRI console [39]. As seen above, the development of MRI technology enables new magnet designs. Hence, to further reduce size and weight of the magnet, we propose a new design and construction method that minimizes large inhomogeneities produced by the short length and material imperfections.

II. METHODS

In this work, we present the design of a low aspect ratio, sparse Halbach magnet for imaging of human extremities. A minimum imaging cross-section of 12.7 cm diameter

was set to accommodate 84% of human ankles [40] in order to meet the requirements of an ankle-size MRI for use on the International Space Station (ISS) as specified by the Canadian Space Agency [41]. The target field strength and homogeneity was selected based on other research that achieved high quality MR images within a Halbach magnet [10], [24]. The size, weight and cost of the magnet were arbitrarily set for this work.

A. THE AIMS OF THE MAGNET DESIGN

1) Magnetic flux density between 50 and 70 mT.
2) Region of interest (ROI) no less than 12.7 cm diameter and 1 cm long cylinder.
3) Homogeneity over ROI better than 12,000 ppm.
4) Magnet inner bore diameter no less than 20 cm.
5) A total magnet weight less than 30 kg.
6) An overall magnet size less than 45 cm × 45 cm × 45 cm.
7) Less than $3000 material costs.

B. MAGNET DESIGN

We used 320 permanent magnet blocks of size 2.54 cm × 2.54 cm × 1.27 cm magnetized along their short axis for the simulations. The blocks were arranged in pairs with a 3 mm spacing, with the blocks magnetization in the same direction, allowing secure mounting (due to their self-attraction) to 3D printed formers [29], [42]. The initial geometry for optimization comprised of 16 block pairs per ring with centers distributed on eight 32 cm diameter rings (Figure 1). Two of the eight rings were nested, consisting of 32 block pairs each, to minimize the impact of field perturbation produced by the finite length of the magnet (see Figure 1B) [12], [13], [15]. The block pairs were evenly spaced by $\Delta\theta = 22.5^0$ ($\Delta\theta = \theta_{i+1} - \theta_i$ where i = 1..16 is the block number; θ is the angle of deviation from the x-axis) to allow enough space for the block pairs radial movement throughout the optimization process (Figure 2). Each block pair magnetization was rotated by $\varphi_i = 270^0 + 2\theta_i$ to generate a dipolar internal magnetic flux density (black arrow in Figure 1A) [43].

Although non-negligible fabrication inconsistency in the size, shape and magnetization of the blocks have been noted by other researchers [9]–[11], [22]–[24], magnetic pieces with minimal fabrication variability are available. There are manufacturers that provide high quality magnetic blocks with very low variances in magnetization strength and direction (<1% and <3°, respectively) as well as very small size variation (<0.1 mm) [44]. For the magnet construction, we used sintered neodymium magnetic pieces type N40UH (N = NdFeB; maximum energy product = 40 MGOe, and maximum material operating temperature (UH) = 180°C) with high coercivity (≥899 kA/m), high remanent fields (12.2 – 12.5 KGs) and low costs (~$4USD/block) [44]. Permanent magnet arrays for MRI commonly use the strongest ferromagnets (N52 grade) since they produce the highest magnetic field strength. Unfortunately, the lower coercivity (≥796 kA/m) of the N52 material

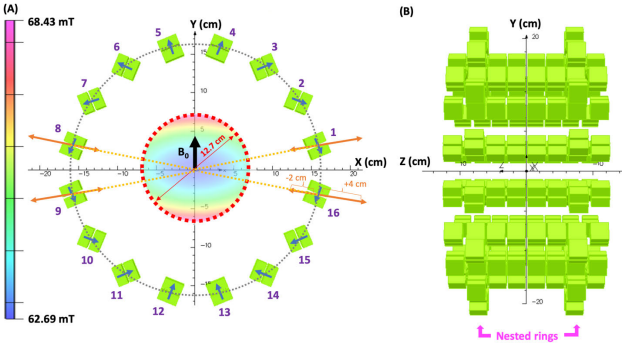

FIGURE 1. The initial geometry of the sparse Halbach magnet. (A) An axial view of one ring showing sixteen block pairs (green) centred on a 32 cm diameter circle (dashed grey). The blue arrows represent the block pair magnetization direction that generates a vertical magnetic field (black arrow). A genetic algorithm was used to find the optimal radial positions of the block pairs (orange arrows). A simulated B_0 map in a central plane shows the low-order field variation in a 12.7 cm diameter area (red dashed circle). (B) A sagittal view of the magnet showing eight coaxial rings 3 mm apart.

contributes to larger (de)magnetization fields caused by an external field [44], [45]. The strong fields produced by blocks in a permanent magnet array effect the magnetization of neighboring blocks and ultimately increase inhomogeneity. Therefore, despite the higher cost and lower remanent field of the N40UH material, we chose to use it because the higher coercivity allows production of a more homogeneous field.

C. MAGNET OPTIMIZATION PROCEDURE

Achieving high homogeneity in a low aspect ratio (less than 1.5:1) Halbach magnet is difficult. The magnet length truncation affects the field homogeneity in an axial plane (see simulated B_0 in Figure 1A). Since the finite length of the magnet is the primary cause for inhomogeneities, we optimized the radial positions of the block pairs in the entire magnet (Figure 1A) [46]. Therefore, as the initial configuration for optimization, we used eight symmetrical rings placed along the z-axis (Figure 1B). Simulations used a B(H) curve provided by a manufacturer for N40UH and optimization of the block pair positions made homogeneity calculations based directly on the simulated field data. A genetic algorithm (GA) was applied to sixteen variables (positions of 4 block pairs per ring × 4 rings) to minimize the difference between the maximum and minimum field within a 12.7 cm diameter and 1 cm thick ROI (Figure 2). The remaining block pairs are symmetrically distributed and optimized; hence no need for simulations. The radial position of each block pair was varied within −2 cm to +4 cm of a 32 cm diameter circle for each ring independently (orange arrows in Figure 1A). In the nested rings, comprising an inner ring distributed at 23.8 cm and outer ring at 40.2 cm, the block pairs sharing a common radial axis were moved simultaneously (Figure 1B). The GA (Global Optimization Toolbox, Matlab, MathWorks, USA) was programmed to generate 100 magnet configurations per generation and 350 generations in total. Regardless of the blocks optimal positions, the magnet geometry maintains an

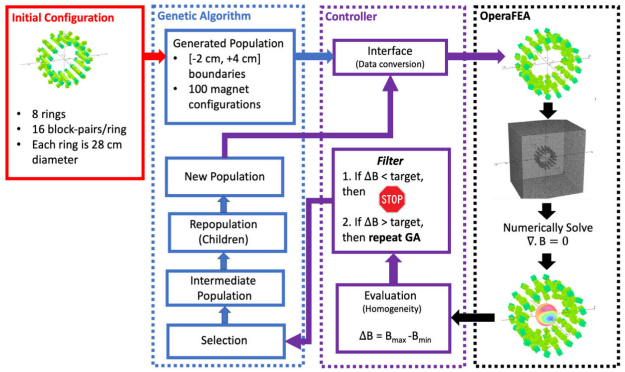

FIGURE 2. The field simulation and optimization data flow. The initial geometry (red) is input into a genetic algorithm that generates 100 random magnet configurations based on the user constraints. A controller of the data flow between the genetic algorithm and finite element magnetostatics (FEM) simulation software was written in Matlab. After a single geometry is simulated, the controller also computes the B_0 homogeneity based directly on the simulated field data and selects configurations based on the most homogeneous fields.

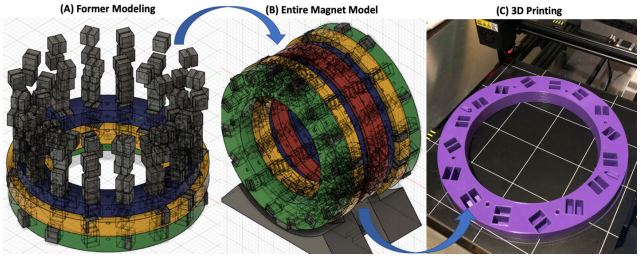

FIGURE 3. Design and construction workflow for ring formers. (A) The computer-aided design modelling of formers for the magnetic blocks. The optimized magnet geometry is cut from the model formers creating pockets in the rings. (B) The entire geometry consists of eight coaxial rings separated by 3 mm in a custom stand. (C) Each ring is 3D printed.

internal diameter of 20 cm, providing sufficient space for RF coils and the imaged object yet constraining the external size to less than 45 cm × 45 cm × 45 cm.

D. MAGNET CONSTRUCTION

Once the optimal positions of the block pairs were determined, the models of each ring were exported directly from Opera3D Modeler (Opera3D, Cobham, UK) to a computer aided design (CAD) software (Autodesk Fusion 360, California, USA). The CAD software was used to generate eight ring formers with specific pockets for the block pairs (Figure 3A). The block sizes were enlarged in the models by 0.18 mm in all directions to compensate for the manufacturing errors of formers and to allow tight fitting. The block models were then subtracted from the ring models to produce cavities for the block pairs. Finally, the former models were converted to a geometry code (i.e. the .gcode file) using slicer software (Cura, Ultimaker, Netherlands) to prepare for 3D printing.

We used polylactic acid (PLA) for 3D printing of the ring formers (Figure 3C and Figure 4a-d) [29], [42]. In the slicer software, we adjusted the settings for the most robust yet lightweight ring formers (octet infill pattern, infill = 20%, wall thickness = 2 mm) [47]. (The profile settings

FIGURE 4. Construction and assembly of the Halbach magnet. Photos of the four (out of 8 total) designed (a-d) and manufactured (e-h) formers. The other four rings (not shown) are identical. The 3D printed formers with N40UH blocks fitted into former pockets are shown. Eight cylindrical (6.35 mm diameter) cuts in the CAD models allow throughput for brass rods, and the pegs/holes in formers minimize ring shifting when compressed. (i-j) Flange brass nuts are tightened, compressing the rings (blue arrows) into their optimized geometry.

used in this work are available upon request.) The block formers were then printed, one at a time, using a 3D printer (Anycubic Chiron, Shenzhen, China) and eight spools of PLA (1.75 ± 0.05 mm, 1 kg spool, Overture3D, USA) in various colors (Figure 4e-h). The total 3D printing time for all the formers was ∼652 hours. Using these profile settings, the weight of each 3D printed ring was ∼0.4 kg and each nested ring ∼0.8 kg. After each print, the ring thickness, block pair pocket spacing, and size were measured with a caliper (Digital Caliper, Tacklife, USA) to ensure less than 0.2 mm deviations from the original CAD models. Any remaining imperfections in the formers were sanded using a multi-function rotary tool (Tacklife Rotary Toolkit, Tacklife, USA). In addition, 3D printed plugs, using PLA, were fitted into the remaining space of the former pockets to minimize shifts during assembly and transportation.

The magnetization direction of each block was measured using a 3-axis Hall probe (THM1176, MetroLab, Switzerland) and marked before fitting blocks into the formers (Figure 4e-h). Beginning with the back-end ring (Figure 4a,e), eight 6.35 mm diameter threaded brass rods were fed through each ring, one at a time, allowing vertical suspension of the rings due to magnetic repulsion. The rings were then compressed (blue arrows in Figure 4j) and tightened with brass nuts in a symmetric fashion analogous to tuning a drum. Compression was considered sufficient when a piece of paper did not slide through the ring gaps. The weakly diamagnetic brass rods and nuts had a negligible

impact on the field and withstands the repulsive forces between rings [22]–[24]. The magnet construction allows disassembling the structure for transportation and shipping.

E. 3D FIELD MEASUREMENTS

The magnetic field produced by the assembled magnet was mapped using a 3-axis Hall probe and computer numerical control (CNC) (Figure 5) [48], [49]. A holder using 3D positioning of the probe was made using commercially available 3D printer hardware railing and a modified 3-axis CNC gantry (Shapeoko 2, Carbide 3D, USA). The CNC gantry (Figure 5b) was precisely positioned by a programmable Arduino-gShield (Synthetos, Adafruit, USA). The motors were supplied by a 24 VDC power supply (LS150-24, TDK-Lambda Americas Inc., Japan). Although the stepper motor accuracy was considered sufficient (∼1 mm), improved calibrations such as micro-stepping could further increase positioning accuracy [49]. The Hall probe was attached to the gantry head through a 9.5 mm aluminum tube. The automation was achieved by combining and modifying open-source Application Program Interfaces (APIs) that were built specifically for the THM1176 Hall probe [50] and GRBL-based CNC controllers [51]. The cardinal axis of the Hall probe was aligned with the field direction to maximize measurement accuracy (0.3 G). Additionally, the Hall probe was triggered to obtain 30,000 averages per measured point (6800 samples per second), increasing measurement precision to 0.02 G. The field measurements and positioning of the probe were automated using an in-house Python code (available at [52]) to map $|B_0|$ at 3 mm × 3 mm × 1 mm steps over a 13.5 cm × 13.5 cm × 1 cm region centered at the magnet geometric isocenter. A total of 22,275 points were collected to create the 3D map requiring about 30 hours. Other research groups have demonstrated more efficient and very accurate (sub-millimeter) mapping systems with higher current external drivers [49].

From the simulated and measured B_0 maps, peak-to-peak homogeneity (η) was then calculated according to the formula:

$$\eta = \frac{\Delta B}{B_c} \times 10^6 \text{ [ppm]}$$

where ΔB [mT] is the difference between maximum B_0 [mT] and minimum B_0 [mT] in the ROI, and B_c [mT] is the magnetic flux density at the geometric isocenter of the magnet.

III. RESULTS

A. FINAL SIMULATED MAGNETIC FIELD

A significant improvement in the simulated homogeneity (11451 ppm) was achieved from the initial configuration (93473 ppm) within the ROI by optimizing the positions of the block pairs in the Halbach magnet using GA. The simulated field strength varies from 66.73 mT to 67.49 mT over the ROI in the optimized design (Figure 6i, ii). The optimized positions of the block pairs in each ring relative to the initial 32 cm diameter circle are listed in Figure 6iii and illustrated in Figures 6iv-vii. A positive value means that the block pair center is shifted outward from the circle; a negative value means inward shift (i.e. closer to the magnets center axis). The magnet is symmetrical about the z-axis; therefore, blocks in −z mirror those in the +z. In addition, the block pair positions are shown for quadrant I (QI) only since movements in QII, QIII and QIV are symmetric.

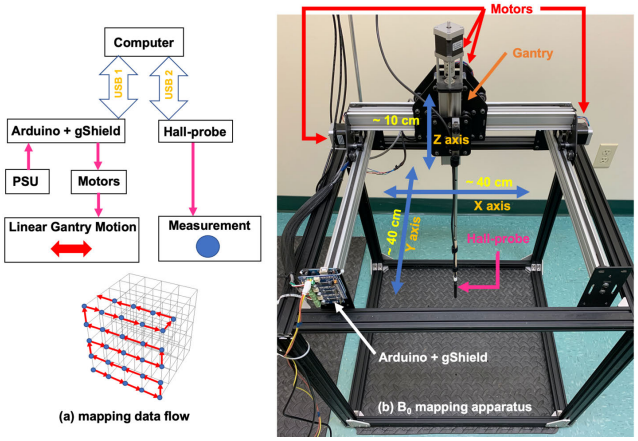

FIGURE 5. The 3D field mapping data flow and apparatus. (a) An in-house Python code was used to stream positional coordinates (g-code) to an Arduino-gShield microcontroller by universal serial bus (USB 1). The g-code is interpreted by the microcontroller and translated into linear motion of the Hall probe in all three dimensions. (b) After a discrete movement, the Hall-probe is triggered to obtain 30,000 magnetic field measurements (B_0). The average magnetic field value is sent back to a computer by a second universal serial bus (USB-2).

B. THREE-DIMENSIONAL MAGNETIC FLUX MAPPING

The longitudinal axis (z) of the constructed magnet was oriented vertically for B_0 mapping (Figure 7A-C). To show minute differences between simulated and measured fields, the simulated (Figure 7D) and measured (Figure 7E) B_0 maps were subtracted for eleven planes ($z = -0.5, -0.4, -0.3, -0.2, -0.1, 0, +0.1, +0.2, +0.3, +0.4, +0.5$ cm). Error maps for three axial planes (out of eleven total) over the ROI are shown in Figure 7F. The error maps reveal that the measured field is lower by 0.21 mT than the simulated field strength within the cylindrical ROI. This deviation is more apparent by comparing projections of the simulated and measured fields along the cardinal axes of the Halbach magnet (Figure 8). The measured field drops 0.21 mT at x = 6 cm (Figure 8a) and 0.17 mT at y = 4.5 cm (Figure 8b).

The simulated and measured B_0 data were then compared to find maximum peak-to-peak field variation ($\Delta B_0 = B_{max} - B_{min}$) within the cylindrical ROI. As seen from Table 1, the measured B_0 homogeneity corresponds to the simulated homogeneity (11451 ppm) within the limited accuracy and precision of the 3D field mapping apparatus.

C. A SUMMARY OF MAGNET SPECIFICATIONS AND COSTS

The simulated and constructed magnet specifications are summarized in Table 1. The final constructed Halbach array

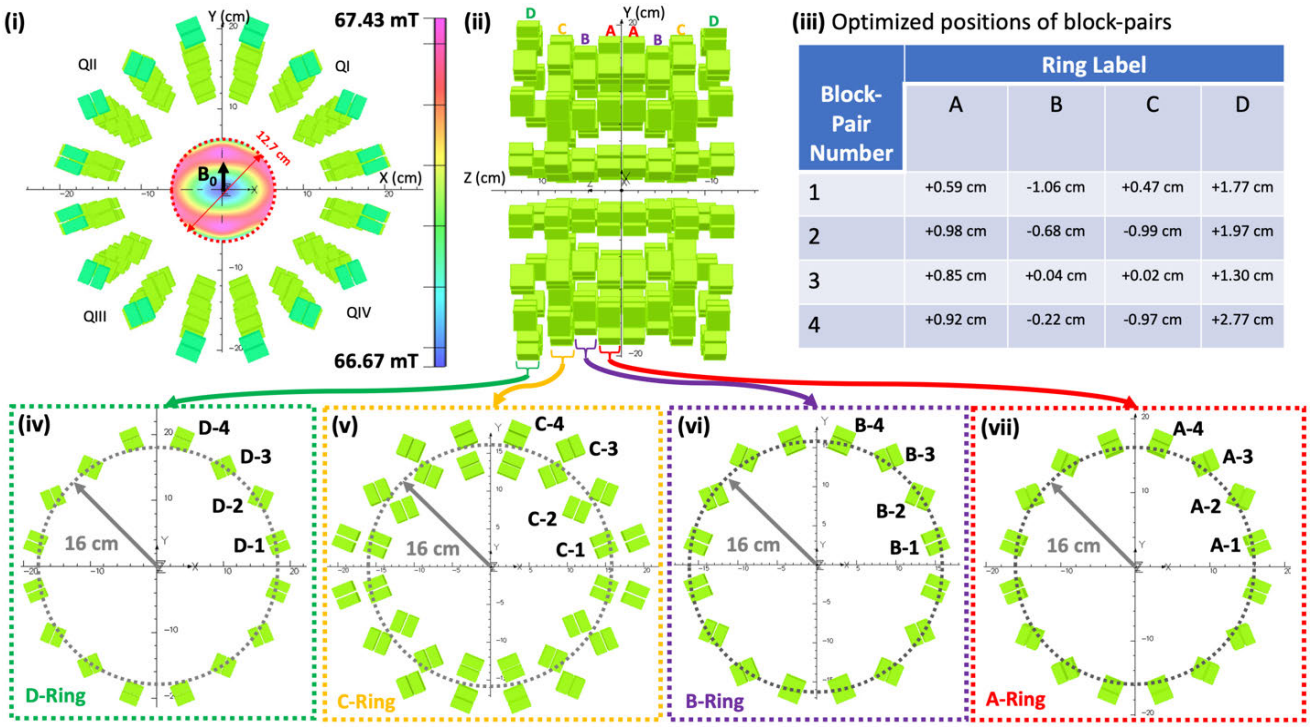

Block-Pair Number	Ring Label A	B	C	D
1	+0.59 cm	-1.06 cm	+0.47 cm	+1.77 cm
2	+0.98 cm	-0.68 cm	-0.99 cm	+1.97 cm
3	+0.85 cm	+0.04 cm	+0.02 cm	+1.30 cm
4	+0.92 cm	-0.22 cm	-0.97 cm	+2.77 cm

FIGURE 6. The final geometry of the sparse Halbach magnet. The block pairs positions were varied in each ring separately for maximum homogeneity in a 12.7 cm diameter, 1 cm long inner cylindrical ROI using the genetic algorithm optimization. (i) An axial view of the optimized magnet showing block pair positions in all eight rings. (ii) A sagittal view of the optimized magnet. (iii) The optimum positions of each block-pair from the initial 32 cm diameter circle. Shifts of the block pair positions are shown only for blocks in the first quadrant (QI) since block shifts in quadrants QII, QIII, and QIV are symmetric. (iv-vii) A visualization of the final block pairs positions for each ring leading to the optimized magnetic field (homogeneity of 11451 ppm) within the cylindrical ROI.

TABLE 1. Comparison of the simulated and measured field strength and homogeneity in the cylindrical region of interest (ROI).

Parameter	Simulated	Measured
B_{max} = Maximum field in ROI [mT]	67.4948	67.4335
B_{min} = Minimum field in ROI [mT]	66.7303	66.6888
$\Delta B = B_{max} - B_{min}$ [mT]	0.7645	0.7447
B_c = Magnetic field at isocenter [mT]	66.7621	66.7768
Homogeneity [ppm]	11451	11152

has a field strength ∼66.7 mT and a measured peak-to-peak homogeneity of 11152 ppm, while simulated homogeneity is 11451 ppm. The constructed magnet has an aspect ratio ∼1:1, overall outer dimensions ∼43 cm × 43 cm × 25 cm, and weight 25 kg (total blocks weight ∼19 kg, formers ∼4 kg, brass rods + nuts ∼2 kg). The material cost is ∼ $2,000 (320 magnets = $1,550, 8 spools of PLA = $240, eight 6.35 mm diameter threaded brass rods = $112, sixteen flange brass nuts = $16).

IV. DISCUSSION

We report a 66.7 mT sparse dipolar Halbach magnet with an aspect ratio of ∼1:1. The new design significantly reduces the weight and size of the sparse Halbach magnet by truncating the magnet length and limiting the imaging volume. The magnet design and its accurate realization removes the technology risk identified by the Canadian Space Agency for MRI magnet designs suitable for use on the ISS [41], [53]–[55]. The 12.7 cm diameter × 1 cm thick ROI disk would allow TRASE imaging of a single slice through an astronaut's leg as specified by the Canadian Space Agency. Although reducing the sensitive volume is not desired, a multi slice technique could be applied by moving the object or the light magnet. The magnet parameters were achieved using permanent magnet blocks type N40UH, with small size variability, and minimal differences in the magnetization direction and strength. The small (de)magnetization offered by N40UH material ensures minimal variations of the magnetization within the magnetic blocks, and ultimately, decreases the discrepancy between the simulated and measured homogeneity. Additionally, we used an accurate B(H) curve of the N40UH material in simulations and used a GA optimization of the block pair positions to achieve maximum field homogeneity.

To ensure magnet durability, lightweight and mechanical strength, the block formers were 3D printed. As visible in Figure 8, there is a small discrepancy (up to 0.21 mT) between the simulated and measured values of the magnetic field. We stipulate that these field deviations are mostly due to the variations in block size, magnetization strength and direction, and the rounded edges of magnets which are not

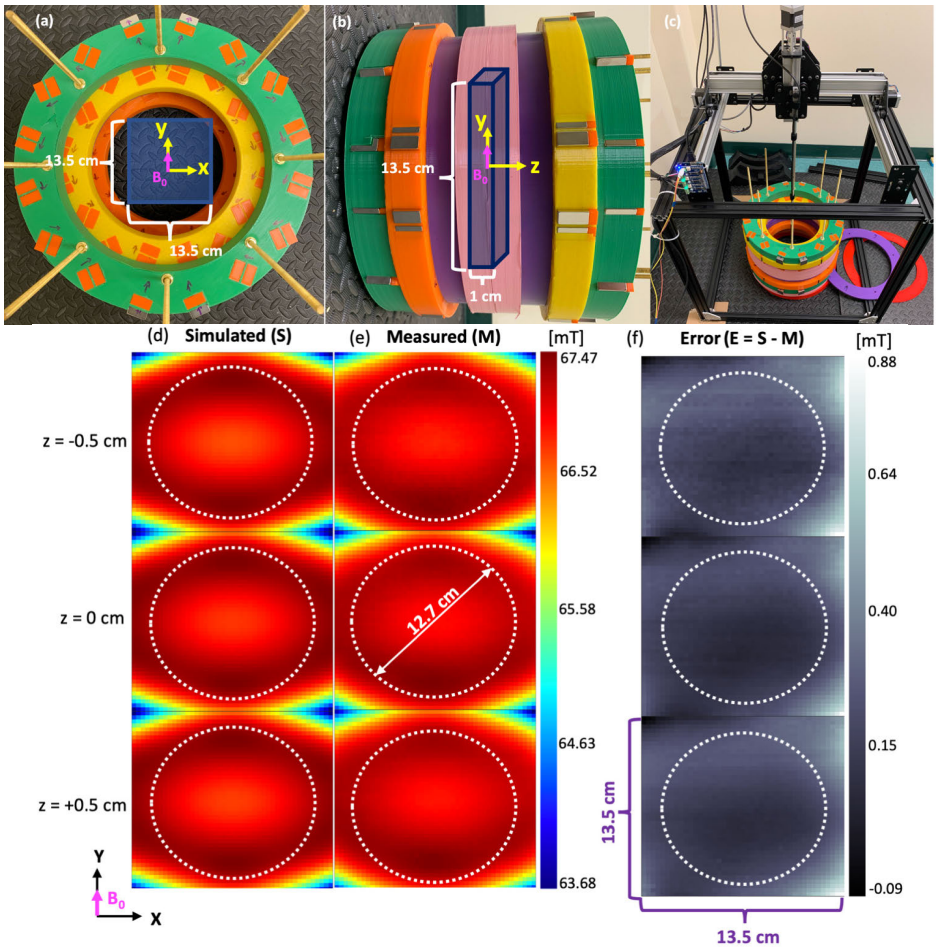

FIGURE 7. The field mapping arrangement and mapping results in the ROI. (a) An axial view of the constructed optimized magnet showing cross-section of the measured region. (b) A sagittal view of the assembled magnet and the measurement volume. (c) The B_0 mapping system automates the magnetic flux density measurements. (d) Simulated (e) Measured and (f) Error maps for the three axial planes over the measured region.

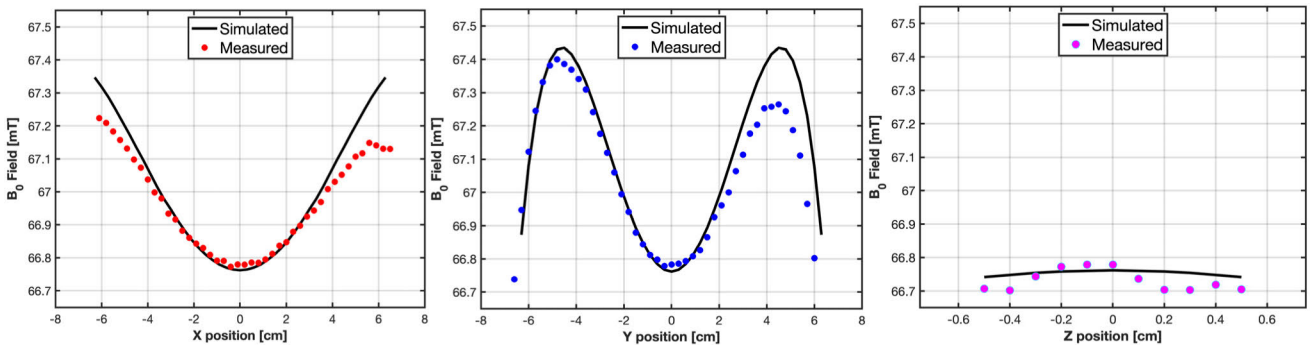

FIGURE 8. The measured and simulated field deviations along the (a) x-axis, (b) y-axis, and (c) z-axis of the Halbach magnet. The measured field deviations from the simulated fields are visible at x = 6 cm and y = 4.5 cm.

modelled in simulations. Asymmetries in x and y directions, visible in Figure 8, are likely caused by the differences of the magnetic fields (strength and direction) in the proximity of the blocks due to imperfections in their production. In addition, inaccuracy (∼0.3 mT) may further influence the field measurements when the magnetic field direction deviates from a cardinal axis of the probe occurring close to the bore surface. Further increase in the measurement accuracy near the inner bore could be achieved by automating rotation of the Hall probe to align with the magnetic

field. Other factors, such as minute differences in tensions between the brass rods and nuts around the circumference of the magnet, temperature instability of ferromagnets and imperfections of the ring formers can also contribute to magnetic field inhomogeneity. Furthermore, the alignment of the B_0 mapping apparatus to the magnet and residual stepper motor imperfections also contribute to systematic errors. Fortunately, the minute decrease of the measured field in these regions has a negligible impact on the actual magnetic field homogeneity despite the typical challenges that disturb field homogeneity in constructed permanent magnet arrays. The presented design could be modified to meet the requirements of specific imaging techniques, such as rotational spatial encoding method (rSEM) or MRI with linear field gradients.

Some MRI applications require higher homogeneity than the constructed Halbach magnet. Fortunately, a five-fold improvement in homogeneity was realized in other sparse Halbach designs by using an array of small-sized permanent magnets [9], [10]. These techniques may be adapted further to improve the field homogeneity of the constructed magnet without losing bore space. In addition, since the magnet rings were compressed, adjustment of rod tensions may also improve magnetic field homogeneity.

V. CONCLUSION

In this work, we simulated the field of a sparse Halbach array and optimized the positions of the blocks in the entire design to reduce dominant magnetic field inhomogeneities caused by the short length of the magnet. Magnetostatics simulation software using finite element analysis and a genetic algorithm optimization in Matlab made homogeneity calculations based directly on the simulated field data. The low magnetic variability between the ferromagnets (N40UH) and the high precision 3D printing of formers allowed to construct a Halbach magnet with parameters matching simulated values. By limiting the imaging volume to a cylindrical region, the length and weight of the magnet was reduced, relative to other approaches. The magnet meets Canadian Space Agency specifications for an ankle MRI for the ISS and the design is suitable for many other low-field portable MRI applications.

ACKNOWLEDGMENT

An abstract for this work was accepted for oral presentation at the International Society for Magnetic Resonance in Medicine (ISMRM) 28th Annual Meeting and Exhibition Online (2020). The authors would like to thank Dr. Cedric Hugon of Hyperfine Research, Inc., for valuable discussion of THM1176 Hall-probe API and triggering. The authors would also like to thank Dr. B. Gino Fallone, Medical Physics Department, Cross Cancer Institute, Edmonton, Alberta, Canada, for access to Opera3D magnetostatics simulation software.

REFERENCES

[1] S. Geethanath and J. T. Vaughan, "Accessible magnetic resonance imaging: A review," *J. Magn. Reson. Imag.*, vol. 49, no. 7, pp. E65–E77, Jun. 2019, doi: 10.1002/jmri.26638.

[2] *Global Atlas of Medical Devices*, World Health Org., Geneva, Switzerland, 2017.

[3] G. I. Ogbole, A. O. Adeyomoye, A. Badu-Peprah, Y. Mensah, and D. A. Nzeh, "Survey of magnetic resonance imaging availability in West Africa," *Pan Afr. Med. J.*, vol. 30, no. 1, p. 240, 2018, doi: 10.11604/pamj.2018.30.240.14000.

[4] L. L. Wald, P. McDaniel, T. Witzel, J. P. Stockmann, and C. Z. Cooley, "Low-cost and portable MRI," *J. Magn. Reson. Imag.*, vol. 52, no. 3, pp. 686–696, 2019.

[5] J. P. Marques, F. F. J. Simonis, and A. G. Webb, "Low-field MRI: An MR physics perspective," *J. Magn. Reson. Imag.*, vol. 49, no. 6, pp. 1528–1542, Jun. 2019.

[6] T. C. Cosmus and M. Parizh, "Advances in whole-body MRI magnets," *IEEE Trans. Appl. Supercond.*, vol. 21, no. 3, pp. 2104–2109, Jun. 2011.

[7] A. J. King, Q. Deng, R. Tyson, J. C. Sharp, J. Matwiy, B. Tomanek, and J. F. Dunn, "*In vivo* open-bore MRI reveals region- and sub-arc-specific lengthening of the unloaded human posterior cruciate ligament," *PLoS ONE*, vol. 7, no. 11, Nov. 2012, Art. no. e48714.

[8] M. Sarracanie and N. Salameh, "Low-field MRI: How low can we go? A fresh view on an old debate," *Frontiers Phys.*, vol. 8, p. 172, Jun. 2020.

[9] T. O'Reilly, W. M. Teeuwisse, and A. G. Webb, "Three-dimensional MRI in a homogenous 27 cm diameter bore Halbach array magnet," *J. Magn. Reson.*, vol. 307, Oct. 2019, Art. no. 106578.

[10] T. O'Reilly, W. M. Teeuwisse, D. Gans, K. Koolstra, and A. G. Webb, "*In vivo* 3D brain and extremity MRI at 50 mT using a permanent magnet Halbach array," *Magn. Reson. Med.*, vol. 85, no. 1, pp. 495–505, Jan. 2021.

[11] C. Hugon, F. D'Amico, G. Aubert, and D. Sakellariou, "Design of arbitrarily homogeneous permanent magnet systems for NMR and MRI: Theory and experimental developments of a simple portable magnet," *J. Magn. Reson.*, vol. 205, no. 1, pp. 75–85, Jul. 2010.

[12] H. Raich and P. Blümler, "Design and construction of a dipolar Halbach array with a homogeneous field from identical bar magnets: NMR mandhalas," *Concepts Magn. Reson. B, Magn. Reson. Eng.*, vol. 23B, no. 1, pp. 16–25, Oct. 2004.

[13] K. Turek and P. Liszkowski, "Magnetic field homogeneity perturbations in finite Halbach dipole magnets," *J. Magn. Reson.*, vol. 238, pp. 52–62, Jan. 2014.

[14] R. C. Jachmann, D. R. Trease, L.-S. Bouchard, D. Sakellariou, R. W. Martin, R. D. Schlueter, T. F. Budinger, and A. Pines, "Multipole shimming of permanent magnets using harmonic corrector rings," *Rev. Sci. Instrum.*, vol. 78, no. 3, Mar. 2007, Art. no. 035115.

[15] T. R. N. Mhíocháin, D. Weaire, S. M. Mcmurry, and J. M. D. Coey, "Analysis of torque in nested magnetic cylinders," *J. Appl. Phys.*, vol. 86, no. 11, pp. 6412–6424, Dec. 1999.

[16] Z. H. Ren, W. C. Mu, and S. Y. Huang, "Design and optimization of a ring-pair permanent magnet array for head imaging in a low-field portable MRI system," *IEEE Trans. Magn.*, vol. 55, no. 1, pp. 1–8, Jan. 2019.

[17] Z. H. Ren, J. Gong, and S. Y. Huang, "An irregular-shaped inward-outward ring-pair magnet array with a monotonic field gradient for 2D head imaging in low-field portable MRI," *IEEE Access*, vol. 7, pp. 48715–48724, 2019.

[18] J. E. Hilton and S. M. Mcmurry, "Halbach cylinders with improved field homogeneity and tailored gradient fields," *IEEE Trans. Magn.*, vol. 43, no. 5, pp. 1898–1902, May 2007.

[19] G. Kustler, "Computation of NdFeB-Halbach cylinders with circular and elliptical cross sections in three dimensions," *IEEE Trans. Magn.*, vol. 46, no. 9, pp. 3601–3607, Sep. 2010.

[20] Q. Chen, G. Zhang, Y. Xu, and X. Yang, "Design and simulation of a multilayer Halbach magnet for NMR," *Concepts Magn. Reson. B, Magn. Reson. Eng.*, vol. 45B, no. 3, pp. 134–141, 2015.

[21] S. Tewari, T. O'Reilly, and A. Webb, "Improving the field homogeneity of fixed- and variable-diameter discrete Halbach magnet arrays for MRI via optimization of the angular magnetization distribution," *J. Magn. Reson.*, vol. 324, Mar. 2021, Art. no. 106923.

[22] C. Z. Cooley, J. P. Stockmann, B. D. Armstrong, M. Sarracanie, M. H. Lev, M. S. Rosen, and L. L. Wald, "Two-dimensional imaging in a lightweight portable MRI scanner without gradient coils," *Magn. Reson. Med.*, vol. 73, no. 2, pp. 872–883, Feb. 2015.

[23] C. Z. Cooley, M. W. Haskell, S. F. Cauley, C. Sappo, C. D. Lapierre, C. G. Ha, J. P. Stockmann, and L. L. Wald, "Design of sparse Halbach magnet arrays for portable MRI using a genetic algorithm," *IEEE Trans. Magn.*, vol. 54, no. 1, Jan. 2018, Art. no. 5100112.

[24] C. Z. Cooley, P. C. McDaniel, J. P. Stockmann, S. A. Srinivas, S. F. Cauley, M. Sliwiak, C. Sappo, C. F. Vaughn, B. Guerin, M. S. Rosen, M. H. Lev, and L. L. Wald, "A portable scanner for magnetic resonance imaging of the brain," *Nature Biomed. Eng.*, vol. 5, no. 3, pp. 229–239, 2021.
[25] K. K. Nielsen, A. R. Insinga, C. R. H. Bahl, and R. Bjørk, "Optimizing a Halbach cylinder for field homogeneity by remanence variation," *J. Magn. Magn. Mater.*, vol. 514, Nov. 2020, Art. no. 167175.
[26] B. Blümich, J. Perlo, and F. Casanova, "Mobile single-sided NMR," *Prog. Nucl. Magn. Reson. Spectrosc.*, vol. 52, no. 4, pp. 197–269, May 2008.
[27] B. Blümich, P. Blümler, G. Eidmann, A. Guthausen, R. Haken, U. Schmitz, K. Saito, and G. Zimmer, "The NMR-mouse: Construction, excitation, and applications," *Magn. Reson. Imag.*, vol. 16, nos. 5–6, pp. 479–484, Jun. 1998.
[28] J. Perlo, F. Casanova, and B. Blümich, "3D imaging with a single-sided sensor: An open tomograph," *J. Magn. Reson.*, vol. 166, no. 2, pp. 228–235, Feb. 2004.
[29] G. E. Sarty and L. Vidarsson, "Magnetic resonance imaging with RF encoding on curved natural slices," *Magn. Reson. Imag.*, vol. 46, pp. 47–55, Feb. 2018.
[30] J. C. Sharp and S. B. King, "MRI using radiofrequency magnetic field phase gradients," *Magn. Reson. Med.*, vol. 63, no. 1, pp. 151–161, Jan. 2010.
[31] J. C. Sharp, S. B. King, Q. Deng, V. Volotovskyy, and B. Tomanek, "High-resolution MRI encoding using radiofrequency phase gradients," *NMR Biomed.*, vol. 26, no. 11, pp. 1602–1607, Nov. 2013.
[32] K. Koolstra, T. O'Reilly, P. Börnert, and A. Webb, "Image distortion correction for MRI in low field permanent magnet systems with strong B_0 inhomogeneity and gradient field nonlinearities," *Magn. Reson. Mater. Phys., Biol. Med.*, Jan. 2021, doi: 10.1007/s10334-021-00907-2.
[33] H. Sun, S. Yong, and J. C. Sharp, "The twisted solenoid RF phase gradient transmit coil for TRASE imaging," *J. Magn. Reson.*, vol. 299, pp. 135–150, Feb. 2019.
[34] H. Sun, A. AlZubaidi, A. Purchase, and J. C. Sharp, "A geometrically decoupled, twisted solenoid single-axis gradient coil set for TRASE," *Magn. Reson. Med.*, vol. 83, no. 4, pp. 1484–1498, Apr. 2020.
[35] A. R. Purchase, T. Pałasz, H. Sun, J. C. Sharp, and B. Tomanek, "A high duty-cycle, multi-channel, power amplifier for high-resolution radiofrequency encoded magnetic resonance imaging," *Magn. Reson. Mater. Phys., Biol. Med.*, vol. 32, no. 6, pp. 679–692, Dec. 2019.
[36] P. Bohidar, H. Sun, G. E. Sarty, and J. C. Sharp, "TRASE 1D sequence performance in imperfect B1 fields," *J. Magn. Reson.*, vol. 305, pp. 77–88, Aug. 2019.
[37] P. Bohidar, H. Sun, J. C. Sharp, and G. E. Sarty, "The effects of coupled B1 fields in B1 encoded TRASE MRI—A simulation study," *Magn. Reson. Imag.*, vol. 74, pp. 74–83, Dec. 2020.
[38] G. E. Sarty, "Natural reconstruction coordinates for imperfect TRASE MRI," *Linear Algebra Appl.*, vol. 611, pp. 94–117, Feb. 2021.
[39] J. C. Sharp, D. Yin, R. H. Bernhardt, Q. Deng, A. E. Procca, R. L. Tyson, K. Lo, and B. Tomanek, "The integration of real and virtual magnetic resonance imaging experiments in a single instrument," *Rev. Sci. Instrum.*, vol. 80, no. 9, Sep. 2009, Art. no. 093709.
[40] *International Space Station Flight Crew Integration Standard (NASA-STD-3000/T)*, Nat. Aeronaut. Space Admin., Revision E, Space Station Program Office, Johnson Space Center, Houston, TX, USA, Jun. 2006.
[41] G. E. Sarty, K. Kontulainen, P. Bohidar, H. Ejalonibu, A. AlZubaidi, L. Vidarsson, G. Warner, P. Piche, M. Mocanita, D. McCabe, P. Cameron, K. Smith, K. Turek, P. Liszkowski, B. Tomanek, H. Sun, A. Purchase, and J. Sharp, "PT11—Magnetic resonance imaging instrument for Ankles," Can. Space Agency, Saint-Hubert, QC, Canada, Tech. Rep. 9F063-160953/011/MTB, 2019.
[42] L. Vidarsson, "Magnetic resonance imaging (MRI) systems and method," U.S. Patent 2015 0 260 809 A1, Sep. 17, 2015.
[43] K. Halbach, "Design of permanent multipole magnets with oriented rare earth cobalt material," *Nucl. Instrum. Methods*, vol. 169, no. 1, pp. 1–10, Feb. 1980.
[44] (Mar. 25, 2021). *BINIC Magnet*. [Online]. Available: http://www.binicmagnet.com/PR01.asp
[45] R. Bjørk, A. Smith, and C. R. H. Bahl, "The efficiency and the demagnetization field of a general Halbach cylinder," *J. Magn. Magn. Mater.*, vol. 384, pp. 128–132, Jun. 2015.
[46] A. R. Purchase, G. E. Sarty, L. Vidarrson, K. Wachowicz, P. Liszkowski, H. Sun, J. C. Sharp, and B. Tomanek, "Design of a permanent magnet for MRI of the ankle on the international space station," *Proc. Int. Soc. Mag. Reson. Med.*, vol. 28, p. 1252, Aug. 2020.
[47] (2021). *All3DP*. Accessed: Mar. 25, 2021. [Online]. Available: https://all3dp.com/2/3d-printer-test-print-10-best-3d-models-to-torture-your-3d-printer/
[48] M. Tallon, G. Scott, M. Dorma, S. Maw, M. Bradley, and G. Sarty, "Compact MRI field mapper," Phys. Eng. Phys. Capstone Project, Univ. Saskatchewan, Saskatoon, SK, Canada, Tech. Rep., 2015.
[49] H. Han, R. Moritz, E. Oberacker, H. Waiczies, T. Niendorf, and L. Winter, "Open source 3D multipurpose measurement system with submillimetre fidelity and first application in magnetic resonance," *Sci. Rep.*, vol. 7, no. 1, Dec. 2017, Art. no. 13452.
[50] C. Hugon. (Mar. 25, 2021). *Python Interface to Metrolab 3 Axis Hall Probe THM1176*. [Online]. Available: https://github.com/Hyperfine/pyTHM1176
[51] J. Sungeun. (Mar. 25, 2021). *GRBL—Simple Gcode Streamer*. [Online]. Available: https://github.com/grbl/grbl
[52] A. R. Purchase. (May 5, 2021). *Three-Dimensional Magnetic Field Mapper (3DFM)*. [Online]. Available: https://github.com/Aaron-Purchase/3DFM
[53] G. E. Sarty, A. Scott, L. Piche, A. McColgan, C. Earnshaw, K. Turek, P. Liszkowski, B. Tomanek, J. Sharp, R. Tyson, K. Lo, V. Volotovskyy, and D. Yin, "Wrist magnetic resonance imager: ISS-MRI," Study Phase, Can. Space Agency, Saint-Hubert, QC, Canada, Final Rep. 9F008A130264/004/MTB, 2014.
[54] G. E. Sarty and A. Obenaus, "Magnetic resonance imaging of astronauts on the international space station and into the solar system," *Can. Aeronaut. Space J.*, vol. 58, no. 1, pp. 60–68, Apr. 2012.
[55] M. Stavnichuk, N. Mikolajewicz, T. Corlett, M. Morris, and S. V. Komarova, "A systematic review and meta-analysis of bone loss in space travelers," *npj Microgr.*, vol. 6, no. 1, p. 13, Dec. 2020, doi: 10.1038/s41526-020-0103-2.

AARON R. PURCHASE received the B.Sc. degree in applied mathematics and Post-Secondary Instructor's Certificate from Memorial University, St. John's, NL, Canada, in 2009 and 2010, respectively, and the B.Sc. degree (Hons.) in physics from the University of Alberta, Edmonton, AB, Canada, in 2016. In 2016, he entered the medical physics M.Sc. program and transferred to the Ph.D. program in 2019. He is currently pursuing the Ph.D. degree with the University of Alberta. From 2012 to 2016, he worked as an Instructor with the Northern Alberta Institute of Technology (NAIT). His research interests include low-field MRI, ultra-light and compact permanent magnet arrays, RF encoding methods, and electronics development.

LOGI VIDARSSON received the B.S. degree from the University of Iceland and the M.S.E.E. and Ph.D. degrees from Stanford University, California. He is currently with LT Imaging. He is the author and coauthor of over a dozen peer-reviewed articles. He holds a patent in the field of magnet design for portable MRI systems. His research interests include portable MRI, magnet design, and development of electronics for portable MRI.

KEITH WACHOWICZ received the B.Sc. degree in engineering physics in 1997, and the Ph.D. degree in medical sciences—biomedical engineering from the University of Alberta in 2004. He is currently an Associate Professor with the Department of Oncology, University of Alberta, and a Medical Physicist at the Cross Cancer Institute. His research interests include rapid real-time MR imaging for therapy guidance, and MRI homogeneity/linearity characterization and geometric correction.

PIOTR LISZKOWSKI received the M.Sc. and Ph.D. degrees in material science from the AGH University of Science and Technology (AGH UST), Kraków, Poland, in 1991 and 1998, respectively.

Since 2006, he has been working with the MRI-Tech Sp. z o.o., Kraków, as a Research Engineer involved in mathematical modeling and calibration of the magnetic fields. He has co-created the analytic methods for rapid designing and optimizing of Halbach dipole magnets made of closely packed blocks. He collaborates with the NMR Imaging Laboratory, Faculty of Physics and Applied Computer Science, AGH UST, in maintenance and development of the demonstration 0.2 T MRI system manufactured by MRI-Tech. He is the coauthor of six peer-reviewed journal articles, four peer-reviewed conference papers, and the author of one peer-reviewed conference presentation.

HONGWEI SUN received the B.Sc. degree in microelectronics from Jilin University in 2014, the M.Sc. degree in medical physics from the University of Manitoba in 2016, and the Ph.D. degree in medical physics from the University of Alberta in 2020. He is currently a Research Collaboration Scientist at United Imaging Healthcare, Beijing, China. His research interests include low-field MRI, PET/MR clinical application, and image-guided radiotherapy.

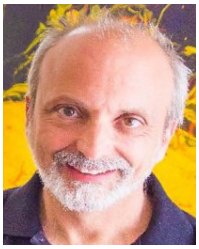

GORDON E. SARTY received the B.Sc. degree in mechanical engineering from the University of New Brunswick in 1982, and the Ph.D. degree in applied mathematics from the University of Saskatchewan in 1995. He is currently a Professor at the University of Saskatchewan. His research interests include fMRI, astrophysics, and developing MRI for use in space.

JONATHAN C. SHARP is currently an Associate Professor with the Department of Oncology, University of Alberta, where he teaches physics in the radiotherapy program. He previously worked for many years at the National Research Council of Canada's Institute for Biodiagnostics, Winnipeg, Manitoba. His research interests include low field MRI technology and the foundations of physics.

BOGUSLAW TOMANEK received the M.Sc. degree in medical physics from the Jagiellonian University, Kraków, Poland in 1988, and the Ph.D. degree in physics from the Institute of Nuclear Physics, Polish Academy of Sciences (IFJ/PAN), Kraków in 1995.

Since 1995, he had worked at IFJ/PAN. From 1998 to 2013, he was a Research Officer with the Institute for Biodiagnostics, National Research Council of Canada. He joined the University of Alberta, Edmonton, Canada, in 2014, where he currently holds a professor position at the Department of Oncology. He is the author of 13 book chapters, more than 140 articles, and seven patents. His research interests include the development of new diagnostic imaging techniques, multimodal imaging, image guided therapy, and application of nanotechnology to medicine.

Dr. Tomanek is a reviewer for over 30 journals, 20 granting agencies, and a member of several societies, including the College of Reviewers and the Canadian Institutes of Health Research. He was a recipient of several awards, including the Outstanding Team Award, the Outstanding Individual Achievement Award, and the Industrial Partnership Award.